Supplement of Weather Clim. Dynam., 5, 609–631, 2024
https://doi.org/10.5194/wcd-5-609-2024-supplement

Supplement of

Exploring the daytime boundary layer evolution based on Doppler spectrum width from multiple coplanar wind lidars during CROSSINN

Nevio Babić et al.

Correspondence to: Nevio Babić (nevio.babic@crocontrol.hr)

1 Spectrum width post-processing and merging

Turbulent Doppler spectrum broadening σ_t^2 can be defined as follows (Smalikho et al., 2005; Wildmann et al., 2019):

$$\sigma_t^2 = \sigma_{sw}^2 - \sigma_0^2 - \sigma_s^2 - E, \tag{1}$$

where σ_{sw}^2 is the measured spectrum width, σ_0^2 equals the spectrum width at constant wind speed within the sampling volume, σ_s^2 is the spectrum width due to shear effects, and E is the random error. During CROSSINN, no raw spectra data were stored primarily due to limitations in data storage capacity. Therefore, we resort to the spectrum width values, as outputted by the WLS200s internal software package Windforge. Although these products have σ_0^2 accounted for, they haven't been corrected for shear effects and random errors (Leosphere, personal communication). As we will demonstrate in the following sections, this incompleteness does not affect the bulk contrasts between turbulent air within the CBL and less turbulent air aloft. Since the post-processing of these outputted spectrum widths requires a different set of criteria for removal of bad data than that for radial velocities (Babić et al., 2021; hereafter B21), in the following we describe these steps in more detail.

To facilitate analyses, for each 1-min RHI scan we first computed the average spectrum width and CNR at each grid point of the coplanar-retrieval mesh which fell within the radius of influence used already for the coplanar retrieval. We determined that for the broad range of conditions encountered during CROSSINN, a more strict CNR criterion was required in case of spectrum width, compared to radial velocities, to filter out general outliers within an RHI scan. Specifically, we filtered out all values with CNR less than -24 dB, compared to -28 dB used for radial velocities. We encountered two additional issues which warranted closer inspection and handling.

1.1 Treatment of artificial spectrum width oscillatory patterns

A regular occurrence in the RHI scans performed by the Mairbach WLS200s lidar was the presence of oscillations in the spectrum width with increasing distance from the origin (Fig. S1a), exhibiting a constant wavelength of approximately 400 m as well as a varying amplitude with increasing distance from the Mairbach lidar (Fig. S1b). These artefacts were particularly evident in cases of low ambient turbulent levels, or equivalently, relatively low spectrum width values not exceeding 0.55 m s^{-1}. Highly turbulent regions in the valley atmosphere masked the presence of the oscillations. Despite our exhaustive internal efforts together with the lidar manufacturer, no successful tracing of the origin of these oscillatory artefacts has been accomplished (Leosphere, personal communication). Similar artefacts were also present in the case of the Hochhäuser lidar, but to a far lesser extent. Therefore, we do not correct the Hochhäuser data for these effects.

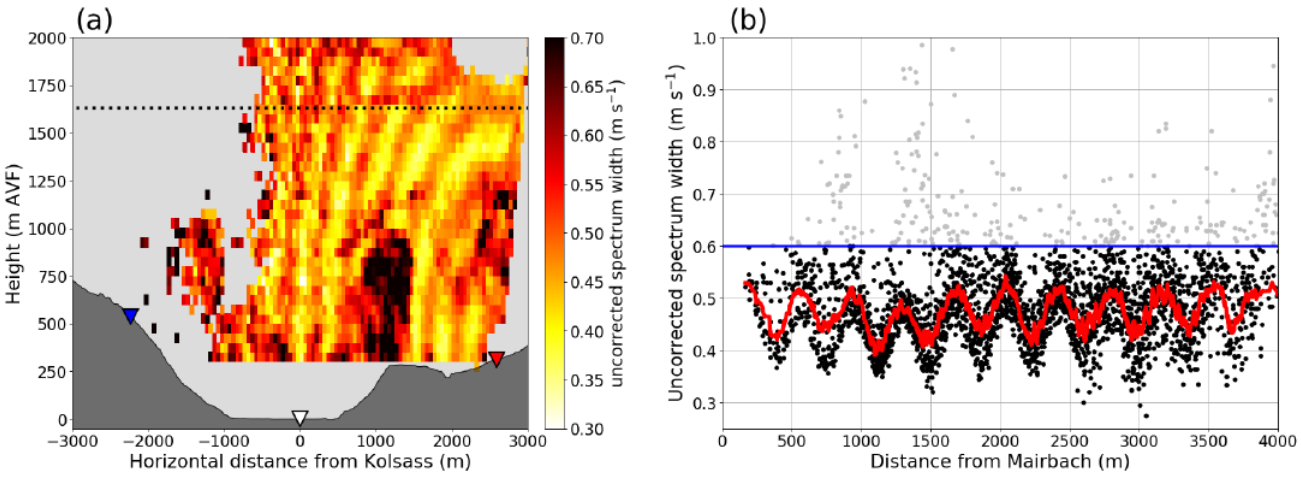

Figure S1: **(a)** Instantaneous two-dimensional representation of the uncorrected spectrum width from the perspective of the WLS200s lidar at Mairbach at 10:58 UTC on IOP 4. **(b)** Uncorrected spectrum width within each grid point of the coplanar retrieval mesh, plotted as a function of its respective distance from the WLS200s lidar at Mairbach, for the same time period as in **(a)**. Grey markers denote the grid points discarded owing to the threshold spectrum width (blue line), while the red line represents the moving average computed based on grid points not discarded by the threshold (black markers), equal to 20 grid points. Coloured triangles, the horizontal dotted black lines, and the N-S orientation of the cross-valley transect in **(a)** are as in Fig. 2 of the main text.

To remove the oscillatory patterns from the Mairbach spectrum width, we first isolated the largest values by imposing a threshold level of 0.6 m s^{-1}. Through examination of several RHIs covering a range of different atmospheric conditions (not shown), we determined that any values beyond this threshold may severely impact the polynomial fitting used to detrend the data distribution in Fig. S1b. These outlier values may be either due to physical phenomena or due to large distances from the origin at Mairbach. The evidence of the former can be found around 1300 m to the south of Mairbach, where the tall column of turbulence is attributed to spectrum width values reaching up to 1 m s^{-1}. On the other hand, the evidence for the latter can be found in case of the grid points also achieving such large spectrum width, but being located over the southern valley sidewall, more than 3500 m away from Mairbach. For our exploration of CBL development, the retaining of the former is highly desirable, while we found that the effect of the latter on the merged spectrum width field is typically not detrimental.

By applying a polynomial moving average with a window size of 20 points to all the spectrum width values not exceeding the threshold of 0.6 m s^{-1}, we have largely isolated the dominant 400-m wavelength of the oscillations while still retaining the smaller-scale perturbations (Fig. S1b). Prior to detrending the valid spectrum width values with this moving average, their mean over the scan is computed and added back to the now detrended spectrum width distribution. The resultant spectrum width field, shown in Fig. S3c, is now sufficiently devoid of any oscillatory artefacts.

Although this approach of removing the oscillations from instantaneous, 1-min RHI scans proved to be plausible, it is not entirely perfect. For instance, note the poor comparison of the fitted polynomial with the spectrum width distribution in the first two troughs, between 200 and 1000 m

away from Mairbach (Fig. S1b). We found that such imperfections tend to get exacerbated with long-term temporal averaging, as evident for instance in Fig. 7g,h,i,l of the main text.

1.2 Addressing the spectrum width range discrepancies between the lidars

Another artificial difference in the spectrum width between the three lidars was the range of values they sampled. On average and compared to Kolsass as the reference data set, the lidar at Hochhäuser systematically sampled the lowest (Fig. S2a), while the lidar at Mairbach systematically sampled the highest spectrum widths (Fig. S2b). To account for this inconsistency and bring the bulk of the distribution of each pair of RHIs as close as possible to the 1-to-1 line on a daily basis (Fig. S2), we computed the medians of both distributions for each day, followed by adding and subtracting the respective median to and from all RHI scans, respectively for Hochhäuser and Mairbach. We found that daytime offsets were sufficiently appropriate for this, furthermore the consideration of all 74 daily offsets for the entire campaign revealed a clear systematic ordering relative to the 1-to-1 line (not shown). From one day to the next, the variability of the daily medians were reflective of the average turbulence intensities sampled on any given day by each of the lidars. Although we also tested hourly offsets, no notable advantages were found compared to the daily approach used here.

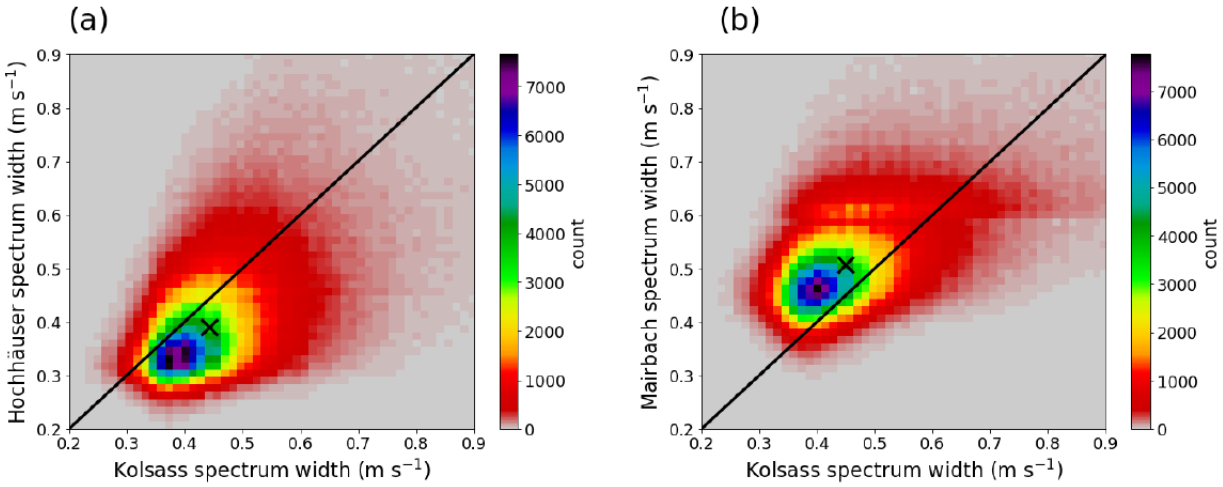

Figure S2: Heatmap representation of uncorrected spectrum widths from the **(a)** WLS200s lidar at Hochhäuser and **(b)** WLS200s lidar at Mairbach, plotted versus the uncorrected spectrum widths from the WLS200s lidar at Kolsass. Matching between the two RHIs is performed for each grid point of the coplanar-retrieval mesh and each 1-min case, for IOP 4 only. The diagonal solid black line represents the 1-to-1 line, while the black cross represents the median of the entire distribution.

1.3 Individual post-processed spectrum width fields

Although the three lidars scanned each section of the valley cross-section at slightly different times within each 1-min period, the agreement in both location and spatial extent of the most prominent post-processed spectrum width features among the three RHIs is encouraging (Fig. 3). This holds

particularly for the features found 1500 m south and 1100 m north of Kolsass. This encouraging degree of stationarity within a single 1-min RHI scan suggests, in turn, a potential benefit from merging together the three separate spectrum width fields. Merging scans in this manner can provide detailed and frequent snapshots of the turbulence state across the whole valley. This merging was done via simple averaging of the three post-processed RHI scans at each grid point of the coplanar retrieval mesh, for each 1-min combination. In the remainder of the study we focus only on the region between the Hochhäuser and Mairbach Doppler lidars (Fig. S2). Due to these two additional post-processing steps, we will hereafter denote the magnitude of spectrum width in arbitrary units (a.u.).

Before proceeding to CBL and MoBL depth detection, it is worthwhile to consider extracting turbulence quantities from several different RHI scans, all with different perspective with respect to the valley atmosphere. In other words, within a highly anisotropic CBL flow, the spectrum width may vary depending on how the laser beam (at a certain elevation of the RHI scan) intersects the flow. Smalikho et al., 2005, in their mathematical considerations of calculating each of the terms that contribute to σ_t^2, assumed purely isotropic turbulence. Nonetheless, they acknowledged that applying their isotropic-based model may be inadequate when the flow is anisotropic and/or inhomogeneous, since different integral scales of turbulence are involved in that case. If indeed significant, we assume that this omission of accounting the effects of RHI intersecting different thermals at different angles does not impact our work, since our instrument setup samples the valley atmosphere from essentially three different angles from below. Although the magnitude of spectrum width might still be affected, we hypothesize that this discrepancy is still much smaller than the magnitude difference of spectrum width between CBL/MoBL and free tropospheric/low-turbulence air aloft, as this contrast is exactly what we rely on in the next section.

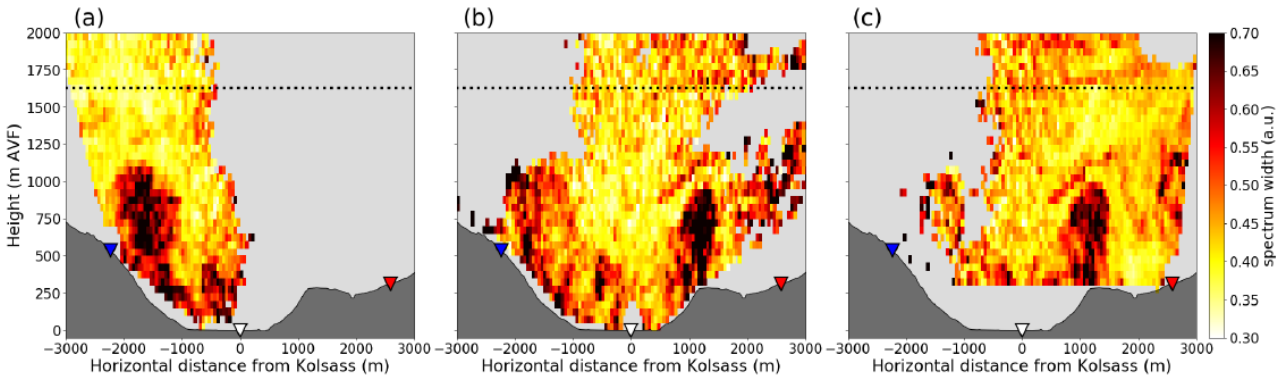

Figure S3: Instantaneous two-dimensional representation of the corrected spectrum width of the WLS200s lidar at **(a)** Hochhäuser, **(b)** Kolsass, and **(c)** Mairbach, valid for 10:58 UTC on IOP 4. Point of view is towards the southwest, i.e. in the upvalley direction. Coloured triangles denote the locations of the WLS200s lidars visible in Fig. 1 of the main text. The horizontal dotted black line indicates the altitude of the average ridgeline level equal to 1630 m above valley floor (AVF).

2 Bottom-up exceedance threshold method for CBL depth z_i determination

As shown in the main text (Section 2.4), the contrast between relatively higher spectrum width values within the CBL compared to those aloft may be utilized to determine the depth of the CBL. We emphasize that this determination was performed on each vertical column of spectrum width in the cross-valley transect, computed as an hourly mean from sixty 1-min instances. Hereafter we apply the method to 1-hr windows shifted 10 minutes forward in time in order to improve temporal resolution and increase visual detail. For instance, a z_i value valid for 12:20 UTC is obtained from a temporal average of all sixty vertical columns of spectrum width at a single horizontal location of the transect between 12:20 and 13:20 UTC.

We found that within the CBL the 1-hr mean spectrum width typically gradually decreases with height until it reaches upper level ambient values of around 0.4 a.u. (e.g. Fig. 6 in the main text), rather than exhibiting abrupt changes near the CBL top that could hint at the entrainment zone. Such gradually decreasing tendency is instead reminiscent of a vertical profile of vertical velocity variance, a common parameter used to infer CBL depths from vertically pointing lidars (Adler and Kalthoff, 2014, their Fig. 2). Therefore, we resorted to a bottom-up exceedance threshold method for determining the CBL depth z_i, leaving us with the task of defining the most appropriate threshold value. For simplicity we will report the CBL depth as z_i, though it may not always correspond to the more traditional definition of CBL depth z_i representing the height of the temperature inversion capping the CBL.

To accomplish z_i estimation, we calibrated the bottom-up method against the bulk-Richardson number method for determining ABL depths from virtual potential temperature θ_v profiles sampled by radiosonde (Kalthoff et al., 2020; Ladstätter, 2020). The bulk-Richardson method relies on targeting the height at which the bulk-Richardson number falls below a widely adopted threshold value of 0.25 (Vogelezang and Holtslag, 1996; Herrera-Mejía and Hoyos, 2019). The bulk-Richardson number R_B equals:

$$R_B = \frac{gz}{\theta_{v,0}} \frac{\theta_v - \theta_{v,0}}{u^2 + v^2}, \tag{2}$$

where g is the gravitational acceleration, z the height AVF, θ_v the virtual potential temperature, $\theta_{v,0}$ the surface virtual potential temperature profile, and u and v the two horizontal wind speed component profiles. We applied the R_B method only to the radiosonde launches performed between 9 and 13 UTC, as this period corresponds to the convectively driven phase (B21; Lehner et al., 2021) when the bottom-up method was observed to perform the best. A possible weakness of the R_B method is its reliance on the accuracy of $\theta_{v,0}$ in highly convective summer conditions. Specifically, owing to the superadiabatic character of the surface layer (Zhang et al., 2014), an unusually deep CBL may be identified, which may have a negative effect on our calibration of the bottom-up method. To establish this tentative influence, we have applied the R_B method to the 9, 11, and 13 UTC radiosonde launches for all ten CROSSINN IOPs, by varying the number of

near-surface data points involved in computing $\theta_{v,0}$.

To identify the optimal spectrum width threshold for the bottom-up method, we computed z_i from all 1-hr spectrum width profiles above Kolsass corresponding to the radiosonde launches for a range of thresholds between 0.38 and 0.47 a.u. These z_i were contrasted against those obtained with the R_B method, for a range of $\theta_{v,0}$ values obtained as averages from the lowest three up to lowest twelve data points of the vertical profile. Given the average spacing between two sounding data points of ten meters, this corresponds to a layer on average between 30 and 120 m thick. For each matching pair of the z_i values from the two methods, the root mean squared error $RMSE$ was computed (Fig. S4) as the most representative statistical parameter to convey the scatter between the two z_i estimates.

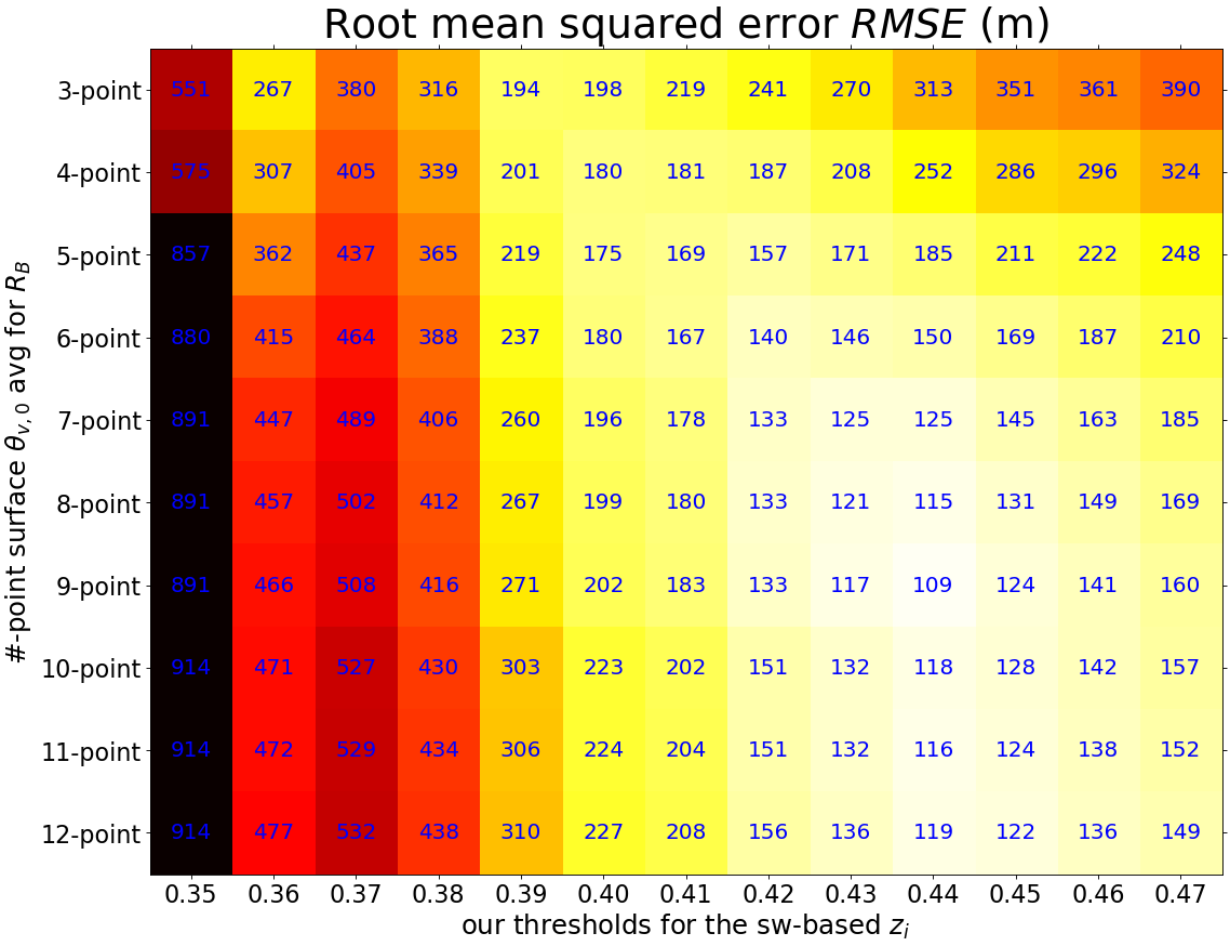

Figure S4: Density heatmap demonstrating the variation of the root mean squared error $RMSE$ of the R_B-based calibration of bottom-up-based z_i estimates. Spectrum width thresholds range from 0.35 to 0.47 a.u., while surface $\theta_{v,0}$ average point number ranges from a 3-point to a 12-point average.

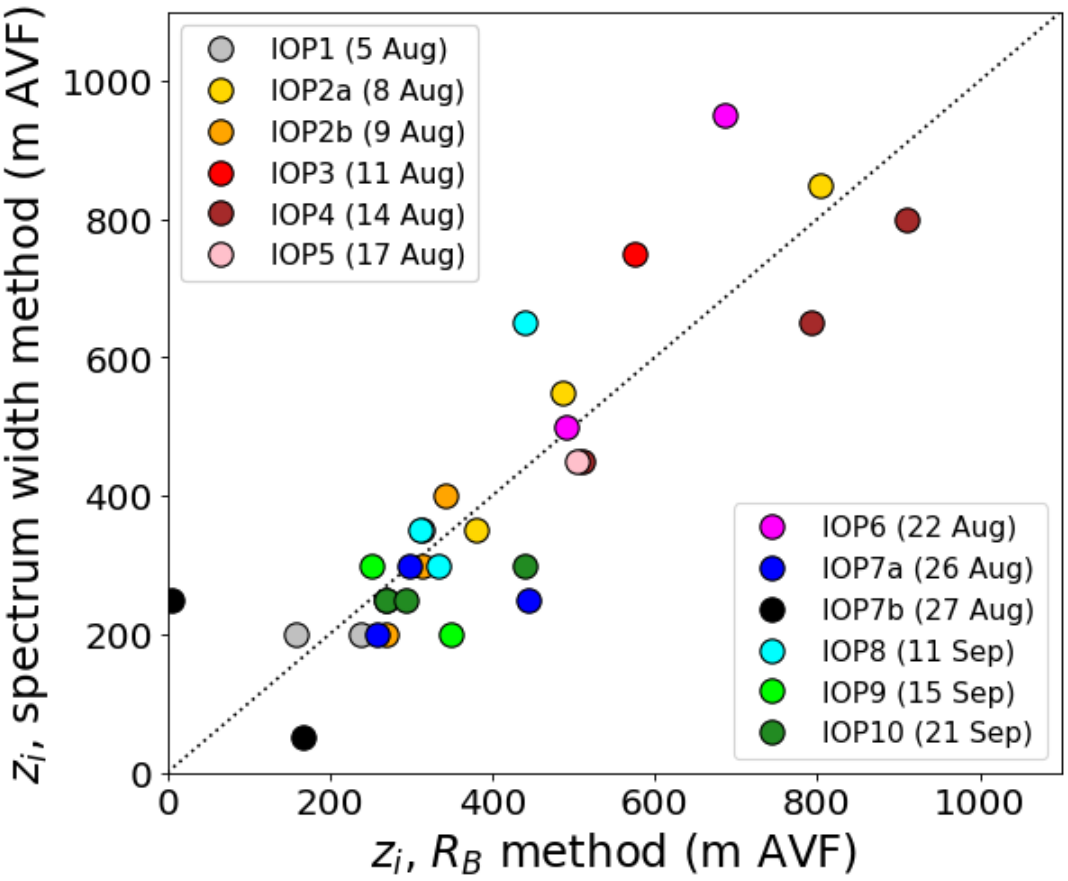

Figure S5: CBL depths z_i obtained with the bottom-up method (threshold equal to 0.44 a.u.) applied to hourly composite merged spectrum width above Kolsass as a function of the z_i obtained with the bulk-Richardson number method applied to the radiosonde virtual potential temperature (threshold equal to $R_B = 0.25$; $\theta_{v,0}$ calculated as the average of the lowest nine data points). Shown are only the radiosonde launch times at 9:00, 11:00, and 13:00 UTC, corresponding to the start of the 1-hour composite merged spectrum width mean. Markers are coloured according to their respective IOP. The thin dotted line represents the 1-to-1 line.

Figure S5, resulting from the choice of 0.44 a.u. threshold and nine data points for the computation of $\theta_{v,0}$, shows the pairing exhibiting the lowest $RMSE$ of all combinations equal to 109 m (Fig. S4), leading us to choose 0.44 a.u. as the final spectrum width threshold. Justified by Fig. S5 and to avoid unreasonably deep z_i, we have imposed an upper limit of 1100 m depth above local topography, beyond which all z_i values have been labeled as erroneous and discarded in the analyses that follow. This specific height threshold was chosen with respect to the negligible chance of a CBL reaching a depth greater than 1100 m (Fig. S5), not just over Kolsass, but in the rest of the cross-section as well. We acknowledge that this, to a certain extent, arbitrarily chosen threshold is far from universal, however it has to be chosen on a per case study basis. No radiosonde-derived z_i were removed with this filter. Furthermore, this filter encapsulates the range of z_i encountered during CROSSINN and for all ten considered IOPs. Nonetheless, there may be instances when the instantaneous, 1-min z_i exceeds this threshold height. One such case, corresponding to a thermal that occurred on IOP 4, depicts the deepest thermal sampled during these four IOPs (Fig. S6), reaching a depth of approximately 1300 m slightly to the southeast of Kolsass. Since this thermal and its advection by the upvalley flow through the RHI plane have ultimately been accounted for

in the calculation of the 1-hr average (which amounted to 850 m AVF), we consider this threshold to be overall sufficiently well suited for the purpose of our study.

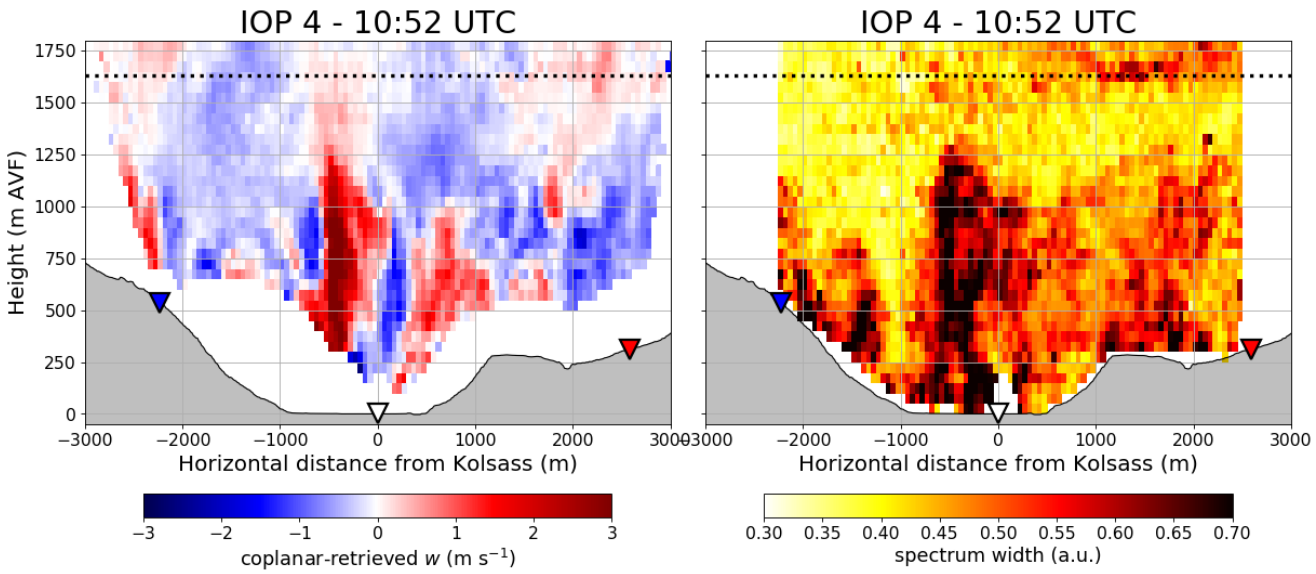

Figure S6: Instantaneous two-dimensional representation of **left** the coplanar-retrieved vertical velocity w, and **right** the averaged merged corrected spectrum width field from the three WLS200s lidars, valid for 10:52 UTC on IOP 4.

As a result, Fig. S5 highlights the rather shallow nature of summer CBLs in the Inn Valley not exceeding more than a kilometre in depth. Seasonality, expressed via progressively lower sensible heat fluxes, is also evident, wherein deeper CBLs occurred during earlier IOPs in August while shallower CBLs were more common during later IOPs in September.

References

Adler, B. and Kalthoff, N.: Multi-scale transport processes observed in the boundary layer over a mountainous island, Boundary-Layer Meteorol., 153, 515–537, https://doi.org/10.1007/s10546-014-9957-8, 2014.

Babić, N., Adler, B., Gohm, A., Kalthoff, N., Haid, M., Lehner, M., Ladstätter, P., and Rotach, M. W.: Cross-valley vortices in the Inn Valley, Austria: Structure, evolution and governing force imbalances, Q. J. Roy. Meteor. Soc., 147, 3835–3861, https://doi.org/10.1002/qj.4159, 2021.

Herrera-Mejía, L. and Hoyos, C. D.: Characterization of the atmospheric boundary layer in a narrow tropical valley using remote-sensing and radiosonde observations and the WRF model: the Aburrá Valley case-study, Q. J. R. Meteorol. Soc., 145, 2641–2665, https://doi.org/10.1002/qj.3583, 2019.

Kalthoff, N., Adler, B., and Bischoff-Gauss, I.: Spatio-temporal structure of the boundary layer under the impact of mountain waves, Meteorol. Z., 29, 409, https://doi.org/10.1127/metz/2020/1033, 2020.

Ladstätter, P.: Vertical structure of the atmospheric boundary layer in the Inn Valley during CROSSINN, Master's thesis, University of Innsbruck, Austria, pp. 114, 2020.

Lehner, M., Rotach, M. W., Sfyri, E., and Obleitner, F.: Spatial and temporal variations in near-surface energy fluxes in an Alpine valley under synoptically undisturbed and clear-sky conditions, Quarterly Journal of the Royal Meteorological Society, 147, 2173–2196, https://doi.org/10.1002/qj.4016, 2021.

Smalikho, I., Köpp, F., and Rahm, S.: Measurement of atmospheric turbulence by 2-μ m Doppler lidar, J. Atmos. Ocean. Technol., 22, 1733–1747, https://doi.org/10.1175/JTECH1815.1, 2005.

Vogelezang, D. and Holtslag, A.: Evaluation and model impacts of alternative boundary-layer height formulations, Boundary-Layer Meteorol., 81, 245–269, https://doi.org/10.1007/BF02430331, 1996.

Wildmann, N., Bodini, N., Lundquist, J. K., Bariteau, L., and Wagner, J.: Estimation of turbulence dissipation rate from Doppler wind lidars and in situ instrumentation for the Perdigão 2017 campaign, Atmos. Meas. Tech., 12, 6401–6423, https://doi.org/10.5194/amt-12-6401-2019, 2019.

Zhang, Y., Gao, Z., Li, D., Li, Y., Zhang, N., Zhao, X., and Chen, J.: On the computation of planetary boundary-layer height using the bulk Richardson number method, Geoscientific Model Development, 7, 2599–2611, https://doi.org/10.5194/gmd-7-2599-2014, 2014.